Hierarchical Multi-Step Folding of Polymer Bilayers

*Georgi Stoychev, Sébastien Turcaud, John W. C. Dunlop, and Leonid Ionov**

A highly complex multi-step folding of isotropic stimuli-responsive polymer bilayers resulting in a variety of 2D and 3D structures is reported. Experimental observations allow determination of empirical rules, which can be used to direct the folding of polymer films in a predictable manner. In particular, it is demonstrated that these rules can be used for the design of a 3D pyramid. The understanding and know-how attained in this study allow the very simple design of highly complex, self-folding 3D objects and open new horizons for 3D patterning, important for the design of microfluidic devices, biomaterials, and soft electronics.

1. Introduction

Nature offers an enormous arsenal of ideas for the design of novel materials with superior properties and interesting behavior. In particular, self-assembly and self-organization, which are fundamental to structure formation in nature, attract significant interest as promising concepts for the design of intelligent materials.[1] Self-folding stimuli-responsive polymer films are exemplary biomimetic materials[2] and can be viewed as model systems for bioinspired actuation. Such films, on one hand, mimic movement mechanisms in certain plant organs[3,4] and, on the other hand, are able to self-organize and form complex 3D structures.[5] These self-folding films consist of two polymers with different properties. Because of the nonequal expansion of the two polymers, these films are able to form tubes,[6,7] capsules[8] or more complex structures.[9] Similar to origami, the self-folding polymeric films provide unique possibilities for the straightforward fabrication of highly complex 3D microstructures with patterned inner and outer walls that cannot be achieved using other technologies.

There are two general approaches for the design of self-folding films. The first approach is based on the use of complexly patterned films, where locally deposited active materials form hinges.[10] Homogenous bilayer films are used in the second approach.[11] Because of the isotropy of the mechanical properties of the bilayer, the formed structures are hinge-free and have rounded shapes. Importantly, in all reported cases, folding runs in one step. On the other hand there are reports that folding in nature can have a very complex character, which strongly depends on the geometry and swelling path[12] that may result in multistep folding (development of curvature in different directions).[3] In this contribution, we demonstrate that the shape of isotropic polymer bilayers is able to direct folding in a sophisticated manner leading to even more complex hierarchical folding than in nature. In particular, films can undergo sequential folding steps by forming various 3D shapes with sharp hinges. By analyzing the folding patterns we elucidated empirical rules, cross-checked by analytical considerations and backed up with finite-element simulations, which allow the folding to be directed, leading to the design of specific 3D shapes. We also highlight the importance of path-dependency in the activation of the actuator, which enables to lock it in a local energy minimum, which can differ from the global one.

G. Stoychev, Dr. L. Ionov
Leibniz Institute of Polymer Research Dresden
Hohe Str. 6, D-01069 Dresden, Germany
E-mail: ionov@ipfdd.de
G. Stoychev
Technische Universität Dresden
Physical Chemistry of Polymer Materials
01062 Dresden, Germany
S. Turcaud, Dr. J. W. C. Dunlop
Department of Biomaterials
Max Planck Institute of Colloids and Interfaces
Am Mühlenberg 1, D-14424, Potsdam, Germany

DOI: 10.1002/adfm.201203245

2. Results and Discussions

For the experiments we used polymer films consisting of two layers of photo-crosslinked polymers: the active layer being a random thermoresponsive copolymer poly(N-isopropylacrylamide-co-acrylic acid) (P(NIPAM-AA) and the passive layer being poly-(methylmethycrylate) (PMMA) (**Figure 1**). The bilayer, prepared as described elsewhere,[7] is located on a silica wafer in such a way that the active and passive polymers are the bottom and top layers, respectively. The bilayer is undeformed in PBS 0.1 M pH = 7.4 environment at T > 70 °C and folding occurs after cooling below 70 °C (Figure 1).

Due to the relatively slow diffusion rate of water inside the P(NIPAM-AA) layer, actuation is driven by the progression of the diffusion front, along which the hydrogel starts to swell. This induces a path-dependency in the folding pattern as the bilayer is not homogeneously activated, but progressively swells as water diffuses from the lateral sides. The investigation of swelling was performed in a qualitative manner by observing the color change of the films which, due to light interference, reflects the change in optical path length (OPL) (**Figure 2**). The OPL varies as a function of the film thickness and refractive index, which in turn depends on the swelling degree.[13] The nonswollen elliptical and star-like films have a homogenous blue (Figure 2a) and reddish (Figure 2d) color, respectively. The difference in the color of both films is caused by their different

© 2013 WILEY-VCH Verlag GmbH & Co. KGaA, Weinheim

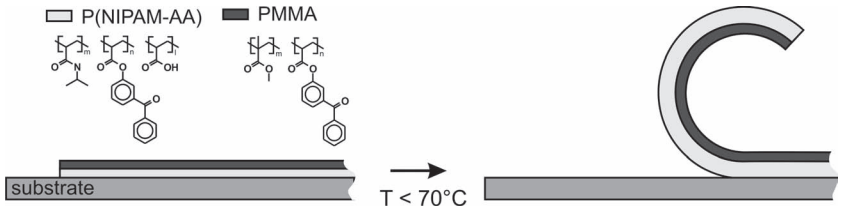

Figure 1. Scheme of folding of a bilayer polymer film consisting of two polymers: hydrophobic PMMA and thermoresponsive hydrogel P(NIPAM-AA).

starting thicknesses (Figure 2). The color of the films starts to change immediately after immersion in water at 25 °C, with the elliptical film becoming redder while the star-like film becomes green (Figure 2b,e). The changes of color in both cases start from the outer periphery of the bilayer film. As the active layer is confined between a water-impermeable silicon wafer and hydrophobic PMMA, this suggests that water can only penetrate inside the layer from the lateral sides.[14] The depth of water penetration along the perimeter of the film (activation depth) is uniform in both cases in the first moments of swelling. The differences in the swelling behavior between the two shapes appear after several seconds of incubation in water. The activation pattern depends on the external shape of the bilayers, with the position of the diffusion front (the activation depth) depending on the distance to the tissue border. This can been seen clearly in the differences of the activation patterns in the convex shapes like ellipse (Figure 2b), and concave ones like star (Figure 2d). For the star-like bilayers, the tips of the triangular-like arms swell faster than their base and their polygonal central part. This can be explained by the fact that after a certain time the diffusion fronts on either side of the arms intersect resulting in faster swelling. The experimental results show that the swelling starts from the periphery of the films and that the activation profile strongly depends on the shape of the film as confirmed by simple finite element simulations (see Figure 2c,f).

We next modeled and experimentally investigated the folding of circular/elliptical and star-like films. Modeling predicts that multiple wrinkles are formed along the perimeter of folding bilayer when it is edge-activated (Figure 2g). The spatial wavelength of the wrinkles is proportional to the activation depth (d) as observed in the wrinkles of leafs due to excessive radial edge-growth[15] and solved analytically in the context of geometrically nonlinear elasticity.[16] As the activation depth increases, the number of wrinkles decreases as P/d, where P is the perimeter of the shape (Figure 2h). The fact that there is both a gradient in radial- (edge-activation) and transversal direction (bilayer), results in a combination of wrinkling and bending, respectively (Figure 2g,h). In full agreement with the modeling predictions, experimental results show that the number of wrinkles decreases during folding (Figure 2i-l). Due to the transversal bending effect, the wrinkles actually evolve into local partial tubes as the activation depth increases. We observed that, at some point, the wrinkles stop to merge and their number remains constant. The probability of merging of two tubes depends on the angle (β, Figure 2h) between them. Experimentally, we found that the critical value of β below which merging of folded tubes was not observed is ca. 120–150°, which corresponds to 6–8 wrinkles when starting with a circular shape (inset in Figure 2h and Figure S3 in the Supporting Information). Based on these experimental observations we derived the first folding rule: "*Bilayer polymer films placed on a substrate start to fold from their periphery and the number of formed wrinkles/tubes decreases until the angle between adjacent wrinkles/tubes approaches 130°*".

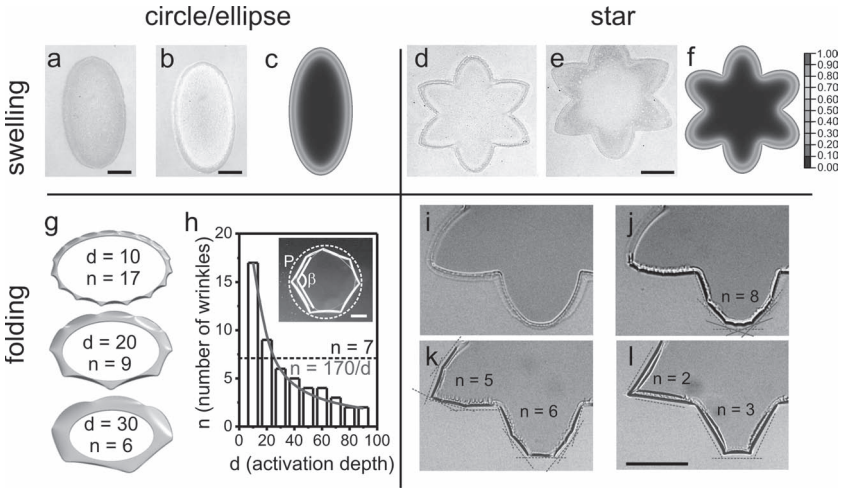

Figure 2. Swelling (upper panels) and first step of folding (lower panels) of circular/elliptical (left panels) and star-like (right panels) bilayer polymer films. a,b,d,e) Microscopy snapshots of swelling elliptical and star-like P(NIPAM-AA)/PMMA bilayers immediately after immersion in water (a,d) and after ca. 60 s incubation (b,e); c,f) Color map of the calculated swelling (from 0 to 1) controlled by water diffusion in the active monolayer with a lateral constant boundary condition (blue is non swollen) dependent on shape obtained by finite element simulations; g) Finite element simulations of wrinkling of a bilayer crown representing the activated edge in case of a circular shape; h) The number of wrinkles is inversely proportional to the actuation depth. Dashed line corresponds to the experimental observation of heptahedrons (inset) when folding is typically stopped in the case of circular shapes. The red line corresponds to n = 170/d. i–l) Two rays of six-ray star during wrinkling, decrease of number of wrinkles is observed. a, b) H_{PNIPAM} = 35 nm, H_{PMMA} = 400 nm; d,e) H_{PNIPAM} = 35 nm, H_{PMMA} = 500 nm; i–l) $H_{(PNIPAM-AA)}$ = 1200 nm, H_{PMMA} = 400 nm, scale bar is 200 µm.

After the number of wrinkles/tubes along the perimeter of the bilayer film stopped to change the bilayers are locked for some time until the subsequent folding step occurs. For example, the wrinkled semi-ellipse bends towards its base (**Figure 3**a). To explain the origin of the second step of folding we considered the geometry of the film after the first folding step. As mentioned, wrinkling of a bilayer leads to the formation of tubes along the perimeter of the film. Considering the fact that the rigidity of the tubes is higher than that of the undeformed films, the polygonal shapes are stiffened by this tube formation, and therefore possess a

© 2013 WILEY-VCH Verlag GmbH & Co. KGaA, Weinheim

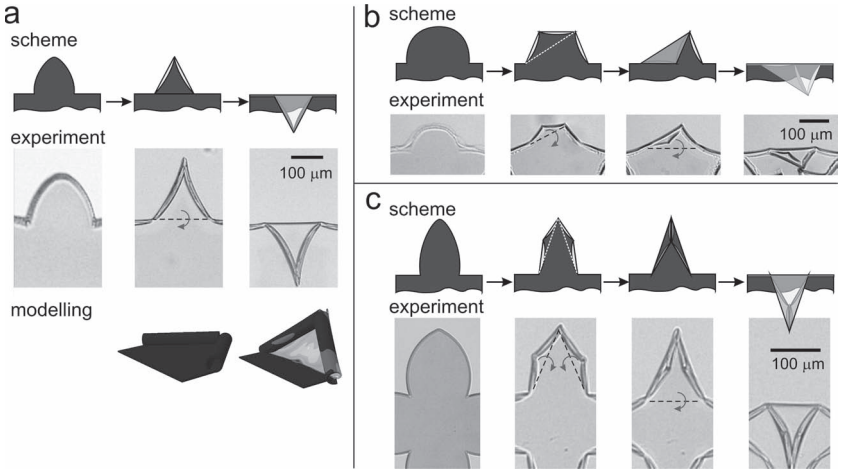

Figure 3. Schematic illustration, experimental observation, and modeling of the second step of folding of the elliptical arms depending on their shape. a) $H_{(PNIPAM-AA)}$ = 1200 nm, H_{PMMA} = 170 nm; b) ($H_{(PNIPAM-AA)}$ = 1200 nm, H_{PMMA} = 400 nm; c) $H_{(PNIPAM-AA)}$ = 900 nm, H_{PMMA} = 170 nm.

number of weak points located at the intersection of the tubes, i.e., at the vertices. These points act like hinges and folding is only observed along the lines connecting them (dashed line in Figure 3a). The formation of hinges during folding of isotropic bilayers, which to our knowledge has not been reported in the literature, is induced by the progressive activation from the lateral sides and the folded shapes are controlled by the initial shapes of the bilayers. This leads to the second rule of the folding: *"After the wrinkles along the perimeter of the film form tubes, further folding proceeds along the lines connecting the vertexes of the folded film"*.

In case there are more than two hinges in the film, a question arises: upon which connecting line will the folding occur? The number of hinges is largely determined by the shape of the semi-ellipses. The regular semi-ellipse, which has a triangular shape after the first step of folding, simply bends toward the base along the line connecting the two bottom vertexes (dashed line in Figure 3a). If the semi-ellipse is more rounded, it forms a trapezoid after the first-step of folding (Figure 3b). In the second step of folding, the trapezoid bends along one of the lines connecting the opposite top and bottom vertexes (dashed line in the second image from the left in Figure 3b). Next, the formed triangle bends towards its base along the line connecting the two bottom vertexes. The elongated semi-ellipse forms four folds after the first step of folding (Figure 3c). Interestingly, the semi-ellipse folds further along the lines connecting the vertexes at the base and the top vertex and no folding along the lines connecting neither the vertexes of the middle nor the ones at the base is observed. Looking at the evolution of the activation pattern through time (diffusion profile see Figure 2), we observe that the lines connecting the hinges can only be used if they are within the activated pattern (red). Thus, the third rule of the folding states: "*the folding goes along the lines which are closer to the periphery of the films*".

Six-ray stars demonstrate the formation of very complex structures (**Figure 4**). Notably simultaneous folding of all rays is observed very rarely and in most cases triangles (Figure 4g) were formed. We investigated the folding in a time-resolved manner in order to explain the formation of the triangles (**Figure 5**). Similar to the experiment demonstrated in Figure 2, wrinkles get longer and bend transversally into tubes (Figure 5b) thus increasing the rigidity of the ray. Next, one of the rays folds towards the center of the star (II in Figure 5c). Folding of this ray leads to the formation of a rigid semi-rolled tube, which is formed by the folded ray and the tubular shoulders of the adjacent rays (Figure 5c). The angle between the base of the folded ray and the shoulders of the neighboring arms is close to 180° (Figure 5c). In this configuration, the weak points located at the intersection between I–II and II–III has disappeared and rays I and III (Figure 5c) cannot bend anymore. As a result, only three remaining rays (IV, V, VI) can bend. If ray V folds, no additional rays can bend (Figure 4l). If ray IV folds (Figure 5d) ray V is blocked. Finally, ray VI can fold leading to the formation of a triangle (Figure 5e). The discussed principle can be easily applied to understand the formation of the other observed figures (Figure 4c–l, Supporting Information Figure S2 and Figure S3). In fact, several factors can be held responsible for the observed symmetry breaking (rays do not fold at the same time) such as inhomogeneities in the films and shape imperfections resulting in small deviations from the symmetric diffusion profile. Based on these experimental observations, one can derive the fourth folding rule: *"Folding of the rays may result in blocking of the neighboring rays if the angle between the base of the folded ray and the shoulders of the neighboring rays is close to 180°"*.

Finally, we applied the derived rules for the design of truly 3D structures–pyramids. In fact, the reason why six-ray star formed flattened folded structures is their short arms and the hindering of folding of rays. Therefore, in order to fabricate pyramids we increased the relative length of the rays and changed the angle between them by decreasing their number (**Figure 6**a,b). The rays of the fabricated four-ray stars first wrinkle along their perimeter (Figure 6c, d). Four tubes are formed along the perimeter of each ray (first rule, Figure 6c), which then collapse two by two and form triangles (second rule, Figure 6d). Since the angle between the folds located on the shoulders of each ray is considerably smaller than 180°, the folding of rays is not self-interfering (forth rule) and all rays fold in the direction of the center of the star (third rule) thus forming a hollow pyramid (Figure 6e–g) that is supported by simulations (Figure 6h). In fact these rules are also applicable to other shapes such as rectangles. As an example we included two-step folding of rectangles (Supporting Information Figure S4).

We observed that, in general, folding rules are applicable to all thickness (we performed many experiments with different thicknesses). The difference between the thin and thick films are in minor. For example, we observe that when star-like thin fold than all six arms (Figure 4d,k) can fold inside because rigidity of the film is not that high. In the

© 2013 WILEY-VCH Verlag GmbH & Co. KGaA, Weinheim

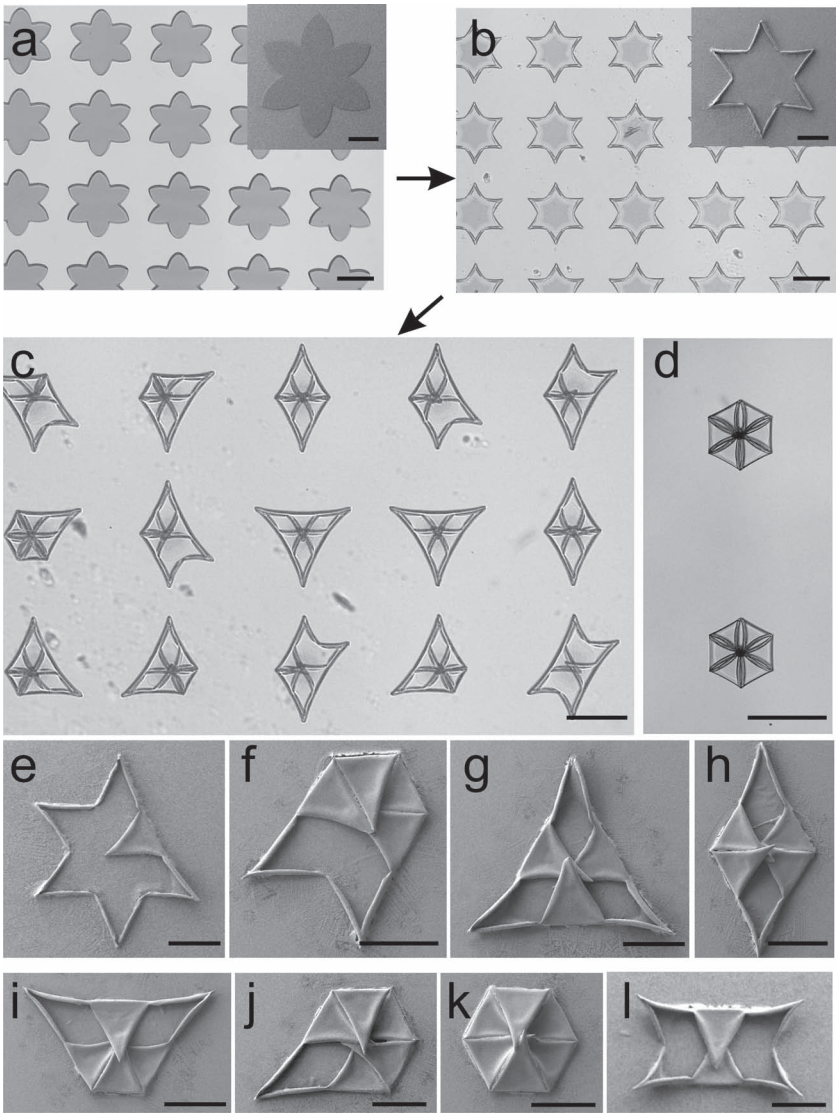

Figure 4. Examples of structures obtained by progressive edge-activation of six-ray star-like bilayers. a) Patterned bilayers; b) First step of actuation: wrinkles collapse into tubes; c–l) Second step of actuation: rays fold leading to several configurations depending on the order of folding. Scale bars are 200 µm, $H_{(PNIPAM-AA)}$ = 1200 nm, H_{PMMA} = 260 nm.

case of thick films, we typically observed folding of 3–4 arms (Figure 4g,l).

3. Conclusions

In conclusion, we investigated the actuation of patterned bilayers placed on a substrate. Due to the edge-activation of the bilayers, the observed deformed shapes differ from the classical ones obtained by homogeneous activation. We found that films can demonstrate several kinds of actuation behavior such as wrinkling, bending and folding that result in a variety of shapes. It was demonstrated that one can introduce hinges into the folded structure by proper design of the bilayer's external shape through diffusion without having to use site selective deposition of active polymers. Experimental observations lead us to derive four empirical rules backed up by theoretical understanding as well as simulations. We then demonstrated how those rules can be used to direct the folding of edge-activated polymer bilayers through a concrete example–the design of a 3D pyramid. We believe that the derived understanding and know-how will allow very simple design of highly complex, self-folding 3D objects and will open new horizons for 3D patterning which is highly important for the design of microfluidic devices, biomaterials, soft electronics, etc.

4. Experimental Section

Materials: *N*-isopropylacrylamide (NIPAM, Aldrich), 4-hydroxybenzophenone (Fluka), polycaprolactone (M_n = 70 000–90 000 Da, Aldrich), benzophenone (Aldrich) and acryloyl chloride (Fluka) were used as received. Methyl methacrylate (MMA, Aldrich) and acrylic acid were purified by filtration through Al_2O_3 column before polymerization.

Synthesis of 4-Acryloylbenzophenone (BA): 4-Hydroxybenzophenone (20 g, 0.1009 mol), diisopropylethylamine (19.3 mL, 0.1110 mol) and 80 mL of methylene chloride were added into 200 mL three-necked round-bottom flask fitted with an overhead stirrer, a thermometer, and an addition funnel with acroloyl chloride (9.02 mL, 0.1110 mol) solution in 20 mL of methylene chloride. The acroloyl chloride solution was added dropwise into the flask under cooling (0–5 °C) for ca 3 h. The methylene chloride was removed by rotary evaporation. The residue was washed with 80 mL of 20% HCl, 80 mL of saturated solution of sodium hydrocarbonate and dried over sodium sulphate. The solution was passed through a silica gel column with chloroform as the eluent. Chloroform was removed by rotary evaporator. Finally, 24.44 g (95%) of ABP was obtained. ^{1}H NMR ($CDCl_3$, 500 MHz): 6.05 (dd, J_1 = 10.40, J_2 = 1.26, 1H), 6.34 (dd, J_1 = 10.40, J_3 = 17.34, 1H), 6.64 (dd, J_3 = 17.34, J_2 = 1.26, 1H), 7.27 (m, 2H), 7.49 (m, 2H), 7.59 (m, 1H), 7.80 (m, 2H), 7.86 (m, 2H).

Synthesis of P(NIPAM-AA-BA): BA (0.28 g, 1,12 mmol); NIPAM (6 g, 51.57 mmol), AA (0.2556 g, 3.36 mmol), AIBN (0.01632 g, 0.38 mmmol) were added in 50 mL flask. Components were dissolved in 30 mL ethanol and degassed with nitrogen for 30 min. The mixture was purged with nitrogen for 30 min. The polymerization was carried at 70 °C under nitrogen atmosphere with mechanical stirring overnight. After cooling, the mixture was poured in 750 mL diethyl ether, the precipitate was filtered and dried in vacuum at 40 °C.

Synthesis of P(MMA-BA): 6.3 g MMA (62.7 mmol), 0.24 g BA (0.96 mmol) and 0.05 g AIBN (0.31 mmol) were dissolved in 30 mL of toluene. The mixture was purged with nitrogen for 30 min. The polymerization was carried at 70 °C under nitrogen atmosphere with mechanical stirring overnight. After cooling, the mixture was poured in 750 mL diethyl ether, the precipitate was filtered and dried in vacuum at 40 °C.

Preparation of Polymer Bilayers: In a typical experiment, poly-(NIPAN-BA) was dip-coated from its ethanol solution on silica wafer substrate. P(MMA-BA) was dip-coated from toluene solution on the

© 2013 WILEY-VCH Verlag GmbH & Co. KGaA, Weinheim

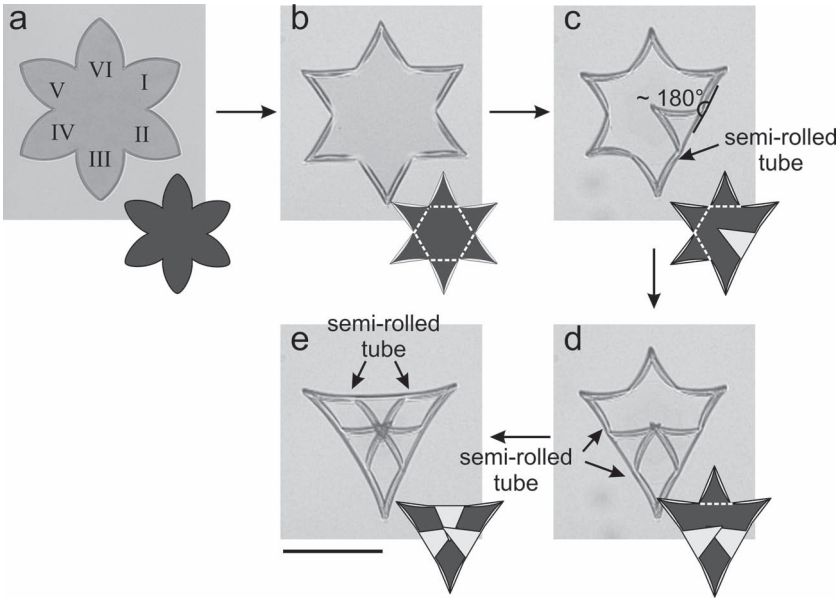

Figure 5. Microscopy snap-shots illustrating the mechanism of formation of triangles during actuation of a six-ray stars. Scale bar is 200 μm, $H_{(PNIPAM-AA)}$ = 1200 nm, H_{PMMA} = 170 nm.

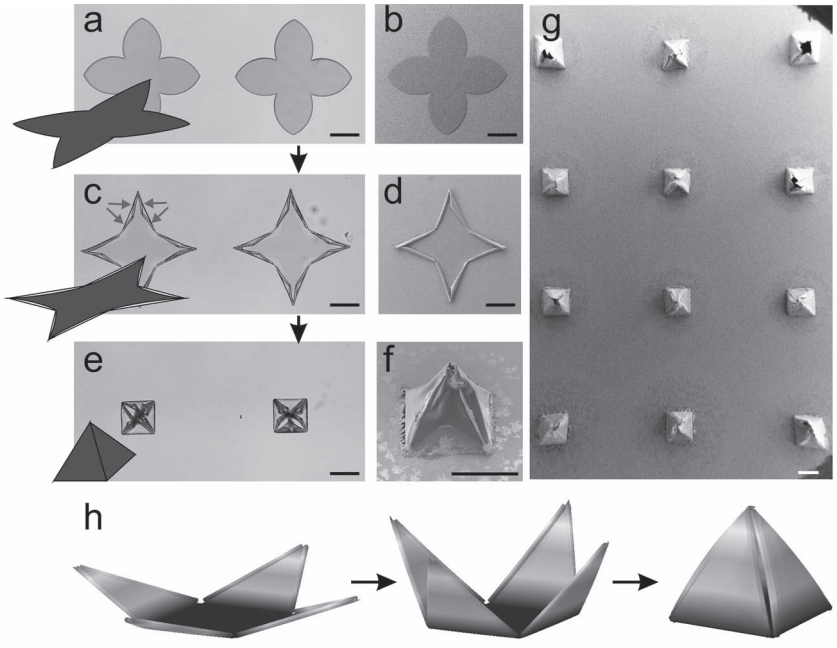

Figure 6. Sequential actuation of four-ray stars leads to the formation of pyramids. a,b) unactivated film; c,d) after wrinkling of the ray periphery into tubes, arrows indicate four wrinkles formed on each arm during first step of folding; e–g) after folding of rays leading to the formation of pyramids. Scale bar is 200 μm, $H_{(PNIPAM-AA)}$ = 1200 nm; H_{PMMA} = 260 nm. h) Simulated folding of four-arm star.

poly-(NIPAM-BA) film. The bilayer film was illuminated through a photomask (Toppan Photomasks inc.) by halogen lamp for 40 min to crosslink the polymers. The illuminated film was rinsed in chloroform in order to remove the polymers from non-irradiated areas. The prepared bilayers were then dried again in air before experiment and contained no water. The observation of bilayer was performed by Axiovert Zeiss Microscope using 5× and 10× air objectives.

Numerical Simulations: Simulations were performed in Abaqus v6.11 using the standard finite-element method. In order to simulate the diffusion process in the active layer we performed a 2D heat transfer analysis with imposed temperature on the free perimeter of the shapes (circle, semi-ellipsoid) and constant diffusive properties This resulted in a time-dependent temperature distribution that mimics the swelling process The resulting nodal temperatures at an early point in time were then applied to the corresponding 3D bilayer shapes having a mismatch in expansion properties (passive layer has 0 thermal expansion, while the active layer has in-plane expansion coefficients of 1). Due to symmetries only the relevant part of the bilayers were simulated in order to reduce computational costs. The resultant actuated shape was obtained through a geometrically nonlinear static step. For more detailed information see ref. [14]. Doing this, we assumed that diffusion-driven actuation follows a quasistatic process in which the timescales of diffusion and actuation are clearly separated. The progression of the diffusion front is slow (s) while the resultant mechanical actuation is fast (ms). This enabled us to consider the two phenomena separately thereby neglecting potential couplings between swelling and mechanical properties. Results are only qualitative, as the actual material characteristics of the hydrogels were not measured. However, the actuation pattern, and thus the number of wrinkles, only depends on the depth of the differential edge-activation named "activation depth" in this paper. This enabled us to predict and confirm the experimental actuation patterns with simple normalized properties.

Supporting Information

Supporting Information is available from the Wiley Online Library or from the author.

Acknowledgements

The authors are grateful to DFG (Grant IO 68/1-1) and IPF for financial support. The authors are grateful to K.-J. Eichhorn and R. Schulze (IPF) for assistance with ellipsometry.

Received: November 5, 2012
Published online: November 26, 2012

[1] a) A. Terfort, N. Bowden, G. M. Whitesides, *Nature* **1997**, *386*, 162; b) G. M. Whitesides, B. Grzybowski, *Science* **2002**, *295*, 2418.
[2] a) T. G. Leong, A. M. Zarafshar, D. H. Gracias, *Small* **2010**, *6*, 792; b) L. Ionov, *Soft Matter* **2011**, *7*, 6786.

© 2013 WILEY-VCH Verlag GmbH & Co. KGaA, Weinheim

[3] M. J. Harrington, K. Razghandi, F. Ditsch, L. Guiducci, M. Rueggeberg, J. W. C. Dunlop, P. Fratzl, C. Neinhuis, I. Burgert, *Nat. Commun.* **2011**, *2*, 337.
[4] a) J. W. C. Dunlop, R. Weinkamer, P. Fratzl, *Mater. Today* **2011**, *14*, 70; b) J. M. Skotheim, L. Mahadevan, *Science* **2005**, *308*, 1308; c) L. Mahadevan, S. Rica, *Science* **2005**, *307*, 1740.
[5] M. Jamal, A. M. Zarafshar, D. H. Gracias, *Nat. Commun.* **2011**, *2*, 527.
[6] S. Zakharchenko, E. Sperling, L. Ionov, *Biomacromolecules* **2011**, *12*, 2211.
[7] S. Zakharchenko, N. Puretskiy, G. Stoychev, M. Stamm, L. Ionov, *Soft Matter* **2010**, *6*, 2633.
[8] G. Stoychev, N. Puretskiy, L. Ionov, *Soft Matter* **2011**, *7*, 3277.
[9] A. Azam, K. Laflin, M. Jamal, R. Fernandes, D. Gracias, *Biomed. Microdevices* **2011**, *1*, 51.
[10] D. H. Gracias, V. Kavthekar, J. C. Love, K. E. Paul, G. M. Whitesides, *Adv. Mater.* **2002**, *14*, 235.
[11] G. S. Huang, Y. F. Mei, D. J. Thurmer, E. Coric, O. G. Schmidt, *Lab Chip* **2009**, *9*, 263.
[12] a) H. Y. Liang, L. Mahadevan, *Proc. Natl. Acad. Sci. USA* **2011**, *108*, 5516; b) H. Liang, L. Mahadevan, *Proc. Natl. Acad. Sci. USA* **2009**, *106*, 22049.
[13] a) I. Jung, J. S. Rhyee, J. Y. Son, R. S. Ruoff, K. Y. Rhee, *Nanotechnology* **2012**, *23*, 025708; b) J. Henrie, S. Kellis, S. M. Schultz, A. Hawkins, *Opt. Express* **2004**, *12*, 1464.
[14] G. Stoychev, S. Zakharchenko, S. Turcaud, J. W. C. Dunlop, L. Ionov, *ACS Nano* **2012**, *6*, 3925.
[15] M. Marder, E. Sharon, S. Smith, B. Roman, *Europhys. Lett.* **2003**, *62*, 498.
[16] B. Audoly, A. Boudaoud, *C. R. Acad. Sci., Ser. IIb: Mec.* **2002**, *330*, 831.

© 2013 WILEY-VCH Verlag GmbH & Co. KGaA, Weinheim